Supplementary Materials for
Quantum Design for Advance Qubits

Feng-Ming Liu[1,2,3], Ming-Cheng Chen[1,2,3], Can Wang[1,2,3], Shao-Wei Li[1,2,3], Zhong-Xia Shang[1,2,3], Chong Ying[1,2,3], Jian-Wen Wang[1,2,3], Cheng-Zhi Peng[1,2,3], Xiaobo Zhu[1,2,3], Chao-Yang Lu[1,2,3], Jian-Wei Pan[1,2,3]

[1]Hefei National Laboratory for Physical Sciences at Microscale and Department of Modern Physics, University of Science and Technology of China, Hefei, Anhui 230026, China [2]Shanghai Branch, CAS Centre for Excellence and Synergetic Innovation Centre in Quantum Information and Quantum Physics, University of Science and Technology of China, Shanghai 201315, China [3]Shanghai Research Center for Quantum Sciences, Shanghai 201315, China

Contents

1. Variational quantum computing of the energy spectrum

1.1 Effect of the photon number truncation

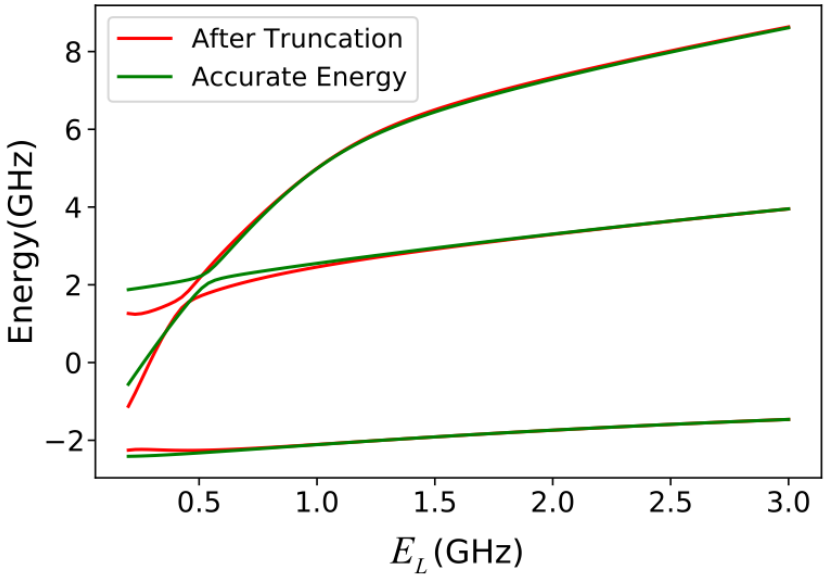

Figure S1. The effect of photon number truncation. The red lines show the energy spectrum when the photon number is truncated to 7 while the green lines represent the accurate energy spectrum.

During the simulation of our quantum electric circuit, we truncated the photon number of quantum states up to 7. The accurate energy spectrum and the energy spectrum obtained after truncation are plotted in Fig. S1. Here, the accurate energy spectrum is calculated by truncating the photon number to 100, in which case the energy error is below 1 MHz and is completely negligible. When we truncate the photon number to 7, the maximum energy error of the lowest three energy states in our simulation range is 171 MHz, 568 MHz and 665 MHz respectively. In both of the energy spectrum we can observe an anti-crossing around 300 MHz, but after truncation its position shifted about 0.1GHz along the axis of E_L. In conclusion, in the range of our simulation, the energy spectrum after truncation has only a slight deviation in the absolute value, without affecting its general profile. Therefore, this truncation will not affect the conclusion of our work.

1.2 Implementation of $\sqrt{iSWAP}$ gates

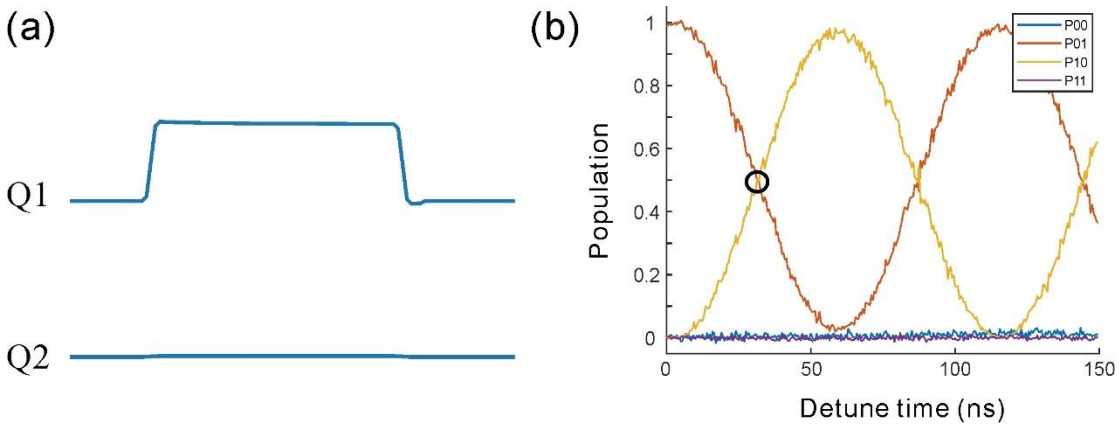

Fig. S2. Implementation of $\sqrt{iSWAP}$ gates. (a) The qubits' bias signal when implementing a $\sqrt{iSWAP}$ gate between Q1 and Q2. (b) The qubits' population as a function of detune time. The black circle indicates the cross of P01 and P10, the detune time of implementing a two-qubit $\sqrt{iSWAP}$ gate is set at this point.

When executing a two-qubit $\sqrt{iSWAP}$ gate, we apply microwave signal to detune the two qubits to the same frequency (Fig. S2a) for a certain time. The length of time is determined according to the Fig. S2b. We initialize Q1 in $|0\rangle$ and Q2 in $|1\rangle$, then we detune then to the same frequency for different time and measure the population of the two qubits. Here, P00 indicates the possibility of the two qubits in $|00\rangle$ and P01 indicates the possibility of the two qubits in $|01\rangle$. And so on. We set the length of detune time at the point where P01 and P10 crosses.

When executing a three-qubit $\sqrt{iSWAP}$ gate, all of the three qubits are detuned to the same frequency. The detune time is determined as follows:

$$t = \frac{1}{1/t_{12} + 1/t_{13} + 1/t_{23}}$$

where t_{12}, t_{13}, t_{23} represents the detune time of $\sqrt{iSWAP}$ gates between the three pairs of qubits Q1-Q2, Q1-Q3 and Q2-Q3. In our experiment, when executing two-

qubit $\sqrt{iSWAP}$ gates between Q1 and Q2, their frequencies are biased to 5.283 GHz and the detune time is 31 ns; when executing three-qubit $\sqrt{iSWAP}$ gates, the frequencies of the three qubits are biased to 5.261 GHz and the detune time is 34 ns.

1.3 Measurement of the Hamiltonian expectation value.

Basis rotation operation	Pauli operators
$Y_{\pi/2} \cdot Y_{\pi/2} \cdot Y_{\pi/2}$	III , IIX , IXX , XIX , XXX
$I \cdot I \cdot I$	IIZ , IZI , ZII
$Y_{\pi/2} \cdot X_{\pi/2} \cdot X_{\pi/2}$	XYY , IYY
$Y_{\pi/2} \cdot I \cdot Y_{\pi/2}$	XZX , IZX
$X_{\pi/2} \cdot Y_{\pi/2} \cdot X_{\pi/2}$	YIY , YXY
$X_{\pi/2} \cdot X_{\pi/2} \cdot Y_{\pi/2}$	YYX
$X_{\pi/2} \cdot I \cdot X_{\pi/2}$	YZY
$I \cdot Y_{\pi/2} \cdot Y_{\pi/2}$	ZXX , ZIX
$I \cdot X_{\pi/2} \cdot X_{\pi/2}$	ZYY
$I \cdot I \cdot Y_{\pi/2}$	ZZX

Table S1. The Pauli operators that constitute the Hamiltonian and the basis rotation operation that required to measure them. The $X_{\pi/2}$ and $Y_{\pi/2}$ here mean rotating the qubit $\pi/2$ along the X and Y axis.

In order to get the expectation of Hamiltonian, we employed the Gray code to map the Hamiltonian into Pauli operators. This mapping is defined as:

$$|0\rangle\langle 1| = (X + iY)/2$$

$$|1\rangle\langle 0| = (X - iY)/2$$

$$|0\rangle\langle 0| = (I + Z)/2$$

$$|1\rangle\langle 1| = (I - Z)/2$$

As a result, the Hamiltonian is represented by a linear combination of Pauli operators represented in Table S1. In our experiment, the Pauli operators that mutually commute are measured simultaneously. Table S1 represents the Pauli operators and the basis rotation operation required to measure them. For example, the expectation value of XXX is measured by rotating each qubit $\pi/2$ along the Y axis (i.e., the basis rotation operation is $Y_{\pi/2} \cdot Y_{\pi/2} \cdot Y_{\pi/2}$) and make measurements for them.

1.4 Characterization of the quantum processor

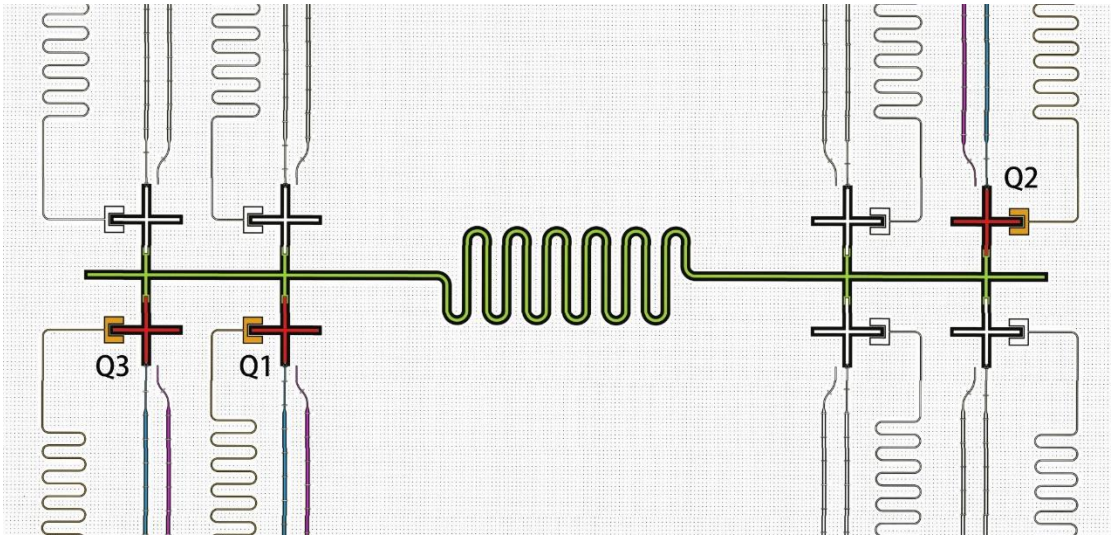

Figure S3. False-color optical image of the quantum processor used in calculation.

As shown in Fig. S3, There are eight Transmon qubits coupled to a common half-wavelength bus resonator (green). In the experiment, we use three of the qubits indicated by red. The qubits are biased by an inductively coupled transmission line (blue) and drived by a capacitively coupled transmission line (purple). Each qubit is coupled to an individual readout resonator (orange) for quantum state readout. The

performance of the three qubits in use is listed in Table S2.

The frequency of the bus resonator is about 5.83 GHz and the coupling strength between qubits and bus resonator is around 50 MHz. The nearest pair of qubits Q1 and Q3 has a direct coupling strength about 2 MHz because of their non-negligible parasitic coupling capacitance.

In order to improve the readout fidelity, we utilized the multi-level readout protocol. When making measurements, we first apply an *X/2* gate to excite the $|1\rangle$ component of quantum state to second excited state $|2\rangle$. This helps reduce the decay error during measurement and therefore improves the readout fidelity.

	Q1	Q2	Q3
f_{01} (GHz)	5.347	5.283	5.212
$f_{01,\mathrm{top}}$ (GHz)	5.349	5.287	5.274
$\eta/2\pi$ (MHz)	241	244	241
T1 (μs)	41	36	28
T2 (μs)	19.5	8.5	1.7
F00 (%)	98.5	98.9	98.7
F11 (%)	95.6	97.4	97.0
X/2 Fidelity (%)	99.75(3)	99.75(4)	99.78(3)

Table S2. Performance of the three qubits used in our experiment. f_{01} is the qubits' idle frequency, $f_{01,\mathrm{top}}$ is the qubits' maximum frequency and $\eta/2\pi$ is the anharmonicity. T1 and T2 is the relaxation time and dephasing time, F00 and F11 is the measurement fidelity when the qubit is prepared in $|0\rangle$ and $|1\rangle$ respectively. *X/2*

Fidelity is the fidelity of *X/2* gate obtained by simultaneous randomized benchmarking of the three qubits.

1.5 Error mitigation based on white noise model

Because of the qubits' finite lifetime, measurement error and other decoherence channels, the final states are not ideal pure states. Here, we model the impurity as white noise, i.e., the experimentally achieved quantum state's density matrix is

$$\rho_{\text{exp}} = p \cdot \rho_{\text{ideal}} + (1-p) \cdot I / d$$

where p is calculated from the purity of the quantum state and d is the dimension of the Hilbert space. In this case, we can make an error mitigation to reduce our experiment error.

$$\langle H \rangle_{\text{ideal}} = \frac{\langle H \rangle_{\text{exp}} - (1-p) \cdot tr(H)/d}{p}$$

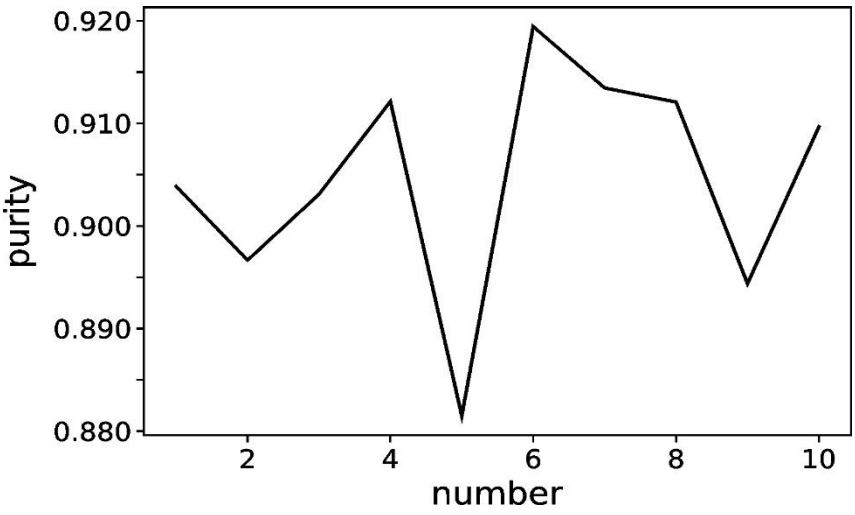

Figure S4. Purity of ten quantum states which is obtained from the same quantum circuit used in the calculation of energy spectrum, but the variational parameters are chosen randomly.

In our work, the purity is estimated from the tomography of ten quantum states which are obtained from the same quantum circuit depicted in Fig. 2B of the main text

and the variational parameters are chosen randomly. The result is shown in Fig. S4. Here, the purity is defined as $tr(\rho^2)$ where ρ is the density matrix.

1.6 Parameters of the qubits in Fig. 3C

Plasmonium	$E_C = 0.60$ GHz, $E_J = 5.61$ GHz, $E_L = 2.20$ GHz
Transmon	$E_C = 0.30$ GHz, $E_J = 14.95$ GHz
Heavy Fluxonium	$E_C = 0.46$ GHz, $E_J = 8.11$ GHz, $E_L = 0.24$ GHz
Quarton	$E_C = 0.97$ GHz, $E_J = 9.95$ GHz, $E_L = 4.58$ GHz

Table S3. List of parameters of the qubits in Fig. 3C

In Fig. 3C of the main text, we compared the flux sensitivity of four types of superconducting qubits. The list of the qubits' parameters is shown in Table. S3. The parameters of the Plasmonium qubit here are the same as those of the experimentally fabricated one that we discussed in this work. To be fair, in the calculation, we set the maximum frequency of the Transmon qubit to be equal with Plasmonium, and the anharmonicity is set to be 300 MHz, which is approximately the largest anharmonicity without affected by charge noise. The parameters of heavy Fluxonium and Quarton are collected from ref. 18 and ref. 19 of the main text. These articles reported the experimentally fabrication of the corresponding type of qubits and above parameters are used.

2. Fabrication and measurement of the Plasmonium qubit

2.1 Sample fabrication

We fabricated four Transmon qubits and four Plasmonium qubits on the same chip as shown in Fig. S5. The results that we present in this work is measured from the Transmon qubit and the Plasmonium qubit which has the best performance.

Our sample is fabricated by the following steps:

(1) A 100 nm thick aluminum film is grown by molecular beam epitaxy (MBE) on a 430 nm sapphire substrate.

(2) The qubit capacitance, transmission lines, readout resonators are fabricated by laser lithography followed by wet etching of the Al film.

(3) SiO_2/Al crossovers are fabricated by lithography followed by lift-off process. We fabricated crossovers every $120\ \mu m$ on transmission lines to elleviate the influence of slotline modes.

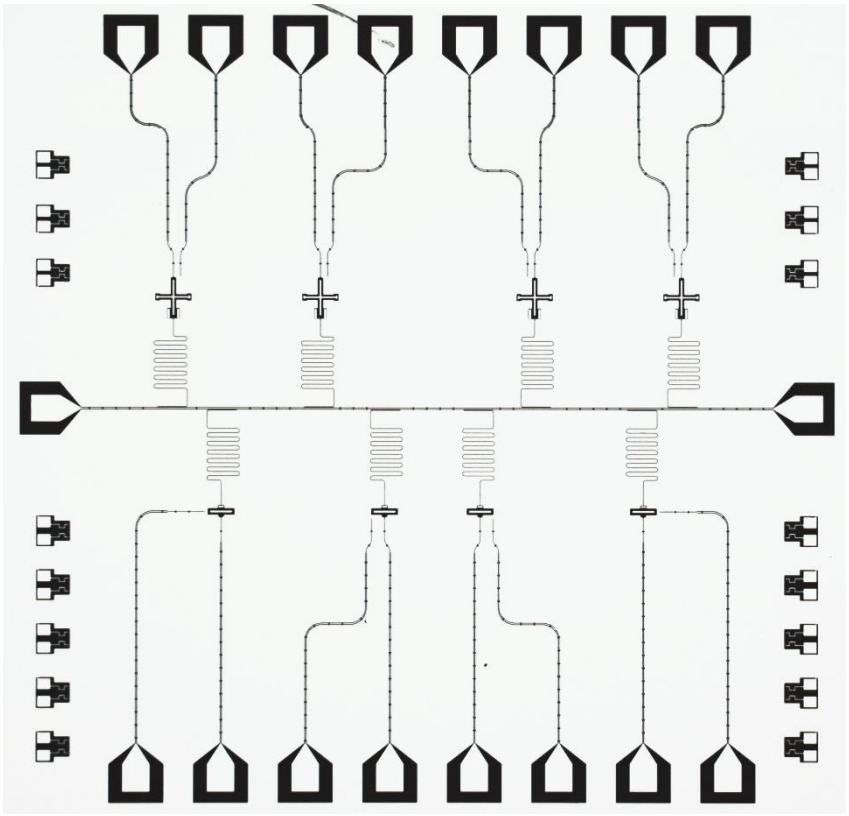

Fig. S5. Optical micrograph of Plasmonium qubits and Transmon qubits fabricated on the same chip.

(4) Josephson junctions, including the Josephson junction array which forms the inductance are fabricated by electron-beam lithography followed by double-angle evaporation and controlled oxidation. With scanning electron microscope, we measured the size of Josephson junction in inductance is $1.3\ \mu m \times 0.3\ \mu m$ and the size of the individual Josephson junction is $0.15\ \mu m \times 0.13\ \mu m$.

2.2 Measurement setup

Our measurement is performed in a dilution refrigerator with a base temperature around 10 mK. A sketch of the measurement setup is shown in Fig. S6. Microwave signals coming in and out of the sample is transmitted by coaxial transmission lines connecting between different temperature stages which is finally wire-bonded to the

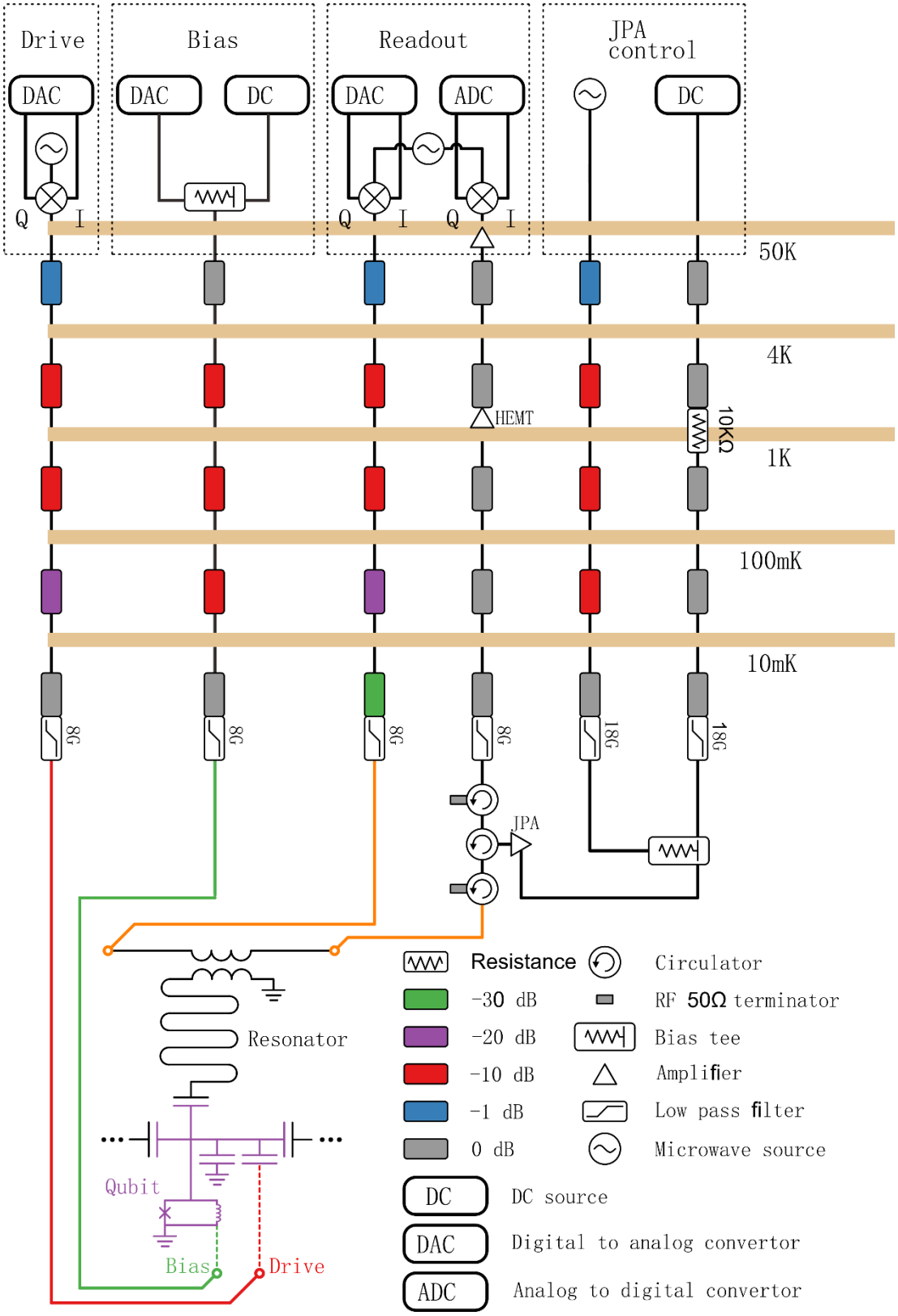

Figure S6. Sketch of the measurement setup of our experiment

digital to analog converter (DAC) and a microwave source via an IQ mixer is applied to the transmission line capacitively coupled to the qubit. In the "Bias" module, a low-frequency microwave signal is applied to the transmission line inductively coupled to the qubit. This low-frequency microwave contains a DC current and a low-frequency signal generated by a digital to analog converter which are mixed at room temperature via a bias tee. In the "Readout" module, a microwave signal is applied to the readout line which is inductively coupled to the readout resonator and the transmitted signal is modulated by an analog to digital converter (ADC) after amplified by a Josephson Parametric Amplifier (JPA) at 10 mK stage, a HEMT amplifier at 4K stage and a low-noise amplifier at room temperature. In order to eliminate thermal noise coming from higher temperature stages, all of the input lines are attenuated by attenuators on different temperature stages and the output of readout signal goes through an array of circulators.

2.3 Origin of the orange dotted line in Fig. 4B

For an ideal microwave generator, the signal of the microwave source $\cos(\Omega t)$ is multiplied by the I channel of DAC: $I = \cos(\omega t + \phi)$ and its quarter-cycle phase shifted signal is multiplied by the Q channel $Q = \sin(\omega t + \phi)$. The output signal is generated by summing the above two results by an IQ mixer:

$$\begin{aligned} output &= \cos(\Omega t)\cos(\omega t + \phi) - \sin(\Omega t)\sin(\omega t + \phi) \\ &= \cos([\Omega + \omega]t + \phi) \end{aligned} .$$

Thus, for an ideal microwave generator, the frequency of output signal is the sum of the frequency of microwave source and the frequency of DAC output. However, for a practical device, the two input channels of IQ mixer I and Q may be imbalanced, which results in an extra output frequency of $\Omega - \omega$. In our experiment, the frequency of microwave source is set to be 5.0 GHz. Therefore, because of the non-ideal microwave drive, there exists an extra spectrum that is symmetrical about 5.0 GHz to the real spectrum.

2.4 Measurement of the Transmon qubit

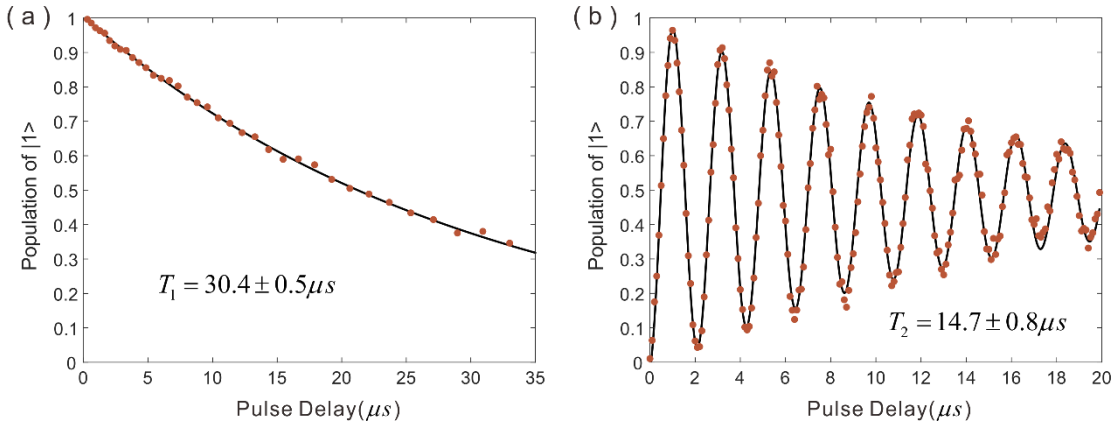

Figure S7. Coherence properties of the Transmon qubit in our sample. (a) Relaxation measurement of the Transmon qubit. (b) Ramsey measurement of the Transmon qubit.

The measured Transmon is fabricated on the same chip together with Plasmonium qubit. Its capacitance is in cross type with a size of $324\ \mu m \times 366\ \mu m$, similar to those used in the quantum calculation of energy spectrum. The charging energy of Transmon is $E_C = 0.24$ GHz and Josephson energy is $E_J = 15.5$ GHz, resulting in an anharmonicity of 240 MHz and transition frequency of $f_{01} = 5.25$ GHz at its flux insensitive point. The measured relaxation time and dephasing time is shown in Fig. S7.

2.5 Extraction of dephasing time by Phase Modulus measurement

Figure S8. The measurement circuit for extracting dephasing time at various detuning points. We first apply an X/2 gate to initialize the qubit in a superposition of $|0\rangle$ and $|1\rangle$, and then bias the qubit to different frequencies for a certain time. Then we bias the qubit back to measure its phase modulus.

Fig. 4C of the main text is obtained by fitting the phase modulus decay with delay time at various detuning points. The measurement circuit is shown in Fig. S8. Here, the phase modulus is measured in the following steps:

(1) Apply a $-Y/2$ gate to the qubit (rotate the qubit 90° counterclockwise around the Y axis of Bloch sphere), then measure the qubit population in $|1\rangle$ (P_1) and $|0\rangle$ (P_0), and record the modulus of their difference $|P_1 - P_0| \equiv M_x$. This is the length of quantum state projection on the *X* axis of Bloch sphere with radius 1.

(2) Apply an $X/2$ gate to the qubit (rotate the qubit 90° clockwise around the X axis of Bloch sphere), then measure the qubit population in $|1\rangle$ (P_1) and $|0\rangle$ (P_0), and record the modulus of their difference $|P_1 - P_0| \equiv M_y$. This is the length of quantum state projection on the *Y* axis of Bloch sphere with radius 1.

(3) Calculate the length of quantum state projection on the *XY* plane of Bloch sphere $\sqrt{M_x^{\,2} + M_y^{\,2}}$, this is what defined as phase modulus PM of a quantum state.

For conventional Ramsey measurement, the qubit is finally rotated around an axis in XY plane whose angle is a dependent of delay time. Therefore, the amplitude of Ramsey fringes is the phase modulus discussed above. In our experiment, we fit the phase modulus decay with delay time with an exponential function $PM = A \cdot \exp(-t/T_2)$, this is equivalent to fitting Ramsey fringes with an exponentially decaying cosine function $P = A + B \cdot \exp(-t/T_2)\cos(\omega t + \phi)$.